ACS Energy LETTERS

http://pubs.acs.org/journal/aelccp

LETTER

Minimizing Recombination at the Perovskite/C_{60} Interface through a Volatile Highly Dense Molecular Interlayer

Fangyuan Ye,△ Shuo Zhang,*,△ Felix Lang, Meysam Raoufi, Jianjun Liang, Igal Levine, Hannes Hempel, Dorothee Menzel, Fengshuo Zu, Steve Albrecht, Lars Korte, Christoph Messmer, Jonas Schön, Stefan W. Glunz, Thomas Unold, Norbert Koch, Dieter Neher, Dongting Ye, Yongzhen Wu,* and Martin Stolterfoht*

Cite This: *ACS Energy Lett.* 2025, 10, 2942−2951

Read Online

ACCESS | Metrics & More | Article Recommendations | Supporting Information

ABSTRACT: **Advancing inverted perovskite solar cells requires effective strategies to mitigate nonradiative recombination at the perovskite/C_{60} interface. Here, we report a volatile material that forms a thin, dense interlayer that essentially eliminates the C_{60}-induced nonradiative interfacial recombination loss despite not directly passivating the perovskite surface. Ultraviolet photoelectron spectroscopy highlights that the molecule forms a positive dipole layer on the surface that aligns the perovskite and C_{60} energy levels for electron conduction. Furthermore, the molecule's volatile nature allows the use of a high-concentration solution that enables a high surface coverage (likely >99%) without increasing the thickness. The combination of these two effects yields an effective approach to suppressing interface recombination. The resulting triple cation perovskite solar cells achieved a power conversion efficiency of >25% and the devices maintain >90% of their initial efficiency after 1200 h of operation. Furthermore, the molecule is broadly applicable to various perovskite compositions and bandgaps.**

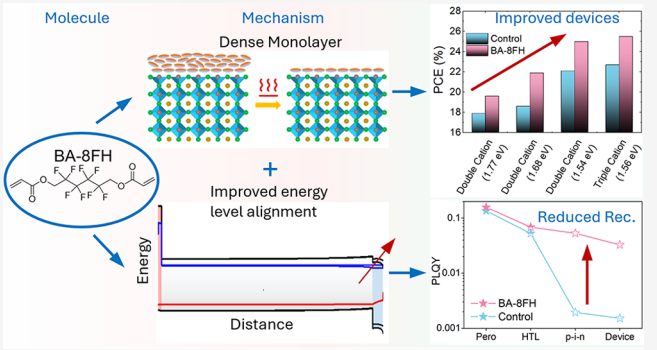

Over the past decade, perovskite-based photovoltaics have emerged as promising PV technology due to their exceptional optoelectronic properties. Single junction perovskite solar cells have demonstrated remarkable progress, with power conversion efficiencies surpassing 26% in both traditional (n-i-p) and inverted (p-i-n) configurations.[1−4] The latter structure has received a lot of attention due to its high commercialization potential, as a result of low-temperature processing, ease of fabrication and upscaling, and high compatibility with perovskite-based tandem devices, which have achieved a remarkable power conversion efficiency (PCE) of over 34%.[5] To realize the full potential of inverted perovskite solar cells, which has been predicted to be around 29% for 1.5 eV perovskite cells and 26% for 1.68 eV cells used for tandem applications,[6,7] it is crucial to delicately manage the perovskite/transport layer interface to minimize nonradiative recombination.

At the buried *p*-interface, the development of self-assembled hole transport layers has led to suppressed nonradiative recombination and prolonged carrier lifetimes. However, the *n*-interface remains a limiting factor for further performance improvements. This stems primarily from the predominant use of fullerene-based electron transport layers (e.g., C_{60} and PCBM), which have been extensively documented to induce nonradiative interfacial recombination. The underlying causes have been widely investigated and are predominantly attributed to interfacial defects or imperfect energy alignment. For example, Warby et al. identified the most substantial loss occurring at the initial monolayer of C_{60}. This suggests that recombination across the interface via C_{60} trap states is the prevailing mechanism, with traps stemming from either charge transfer states or density of states (DOS) broadening at the interface, pinning the lowest unoccupied molecular orbital

Received: February 25, 2025
Revised: May 9, 2025
Accepted: May 12, 2025
Published: May 26, 2025

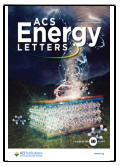

https://doi.org/10.1021/acsenergylett.5c00615
ACS Energy Lett. 2025, 10, 2942−2951

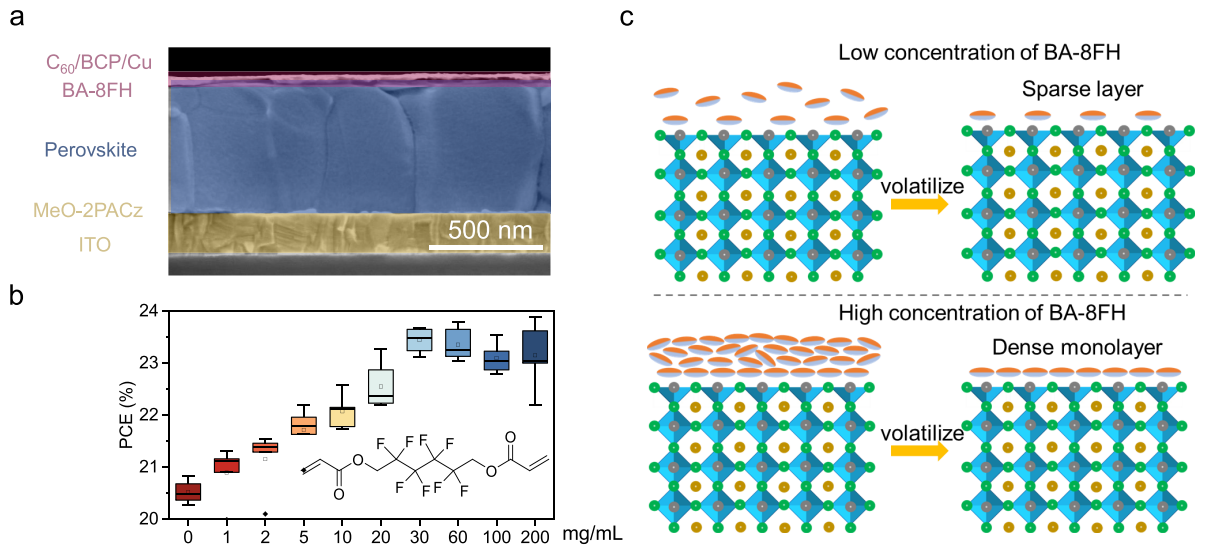

Figure 1. (a) Scanning electron microscope (SEM) image of the cross-section of the complete device with BA-8FH treatment, all layers are labeled on the left. (b) Performance statistics for control and BA-8FH treated devices for increasing concentrations, based on 10 devices per group. (c) Schematic presentation of the possible molecular assembly on the perovskite top surface.

(LUMO) below the conduction band of perovskite.[8] The dominant contribution of C_{60}-induced traps was also suggested by many other authors.[9−11] However, by performing ultrasensitive UPS measurements, Menzel et al. revealed an energy offset of 0.26 eV between the LUMO-edge of C_{60} and the conduction band minimum (CBM) of a 1.64 eV triple cation perovskite ($Cs_{0.05}(FA_{0.83}MA_{0.17})_{0.95}Pb(I_{0.83}B_{0.17})_3$) which could significantly limit the device open-circuit voltage (V_{OC}).[12] Importantly, if the interface with the energy offset is limiting the overall device recombination, the energy level misalignment of majority carriers (E_{maj}) will reduce the V_{OC} directly, while the trap state density (N_t) reduces the V_{OC} only logarithmically in the case of Shockley-Read-Hall (SRH) recombination[13]

$$V_{OC} = 2V_{th}\ln\left(\frac{2G_{ext}}{n_i(N_tC_t)}\right) - \Delta E_{maj} \quad (1)$$

where respectively, V_{th} the thermal voltage, G_{ext} is the generation rate of electron−hole pairs due to external illumination, n_i the intrinsic carrier density, and C_t the capture rate coefficient for charge trapping. We note, an equal electron and hole carrier lifetime ($\tau_{n/p}$) and high-level injection conditions (carrier density at $V_{OC} \gg$ intrinsic carrier density, $n \gg n_0$) have been assumed for simplicity. In other words, this suggests that minimizing the energy level offset is exponentially more important than reducing trap states at the interface. Therefore, aligning energy levels is a pivotal strategy in eliminating the loss pathway at the perovskite/C_{60} interface.

To improve the energy level alignment and optimize the perovskite/C_{60} interface, various interfacial engineering strategies have been incorporated, such as 2D perovskite layers, reactive capping layers, ionic liquids, and insulating polymer layers. However, due to the mostly insulating properties of the materials, which will cause transport loss, the implementation of those strategies generally faces the significant challenge of finding the optimal balance between maximizing the V_{OC} and maintaining a high fill factor (FF). This commonly results in a narrow window for optimization, necessitating precise control of interlayer deposition and thickness, leading to inconsistent reproducibility and increased trial-and-error. Moreover, as we will further discuss in the manuscript, given the long charge carrier diffusion length of perovskite in the μm-range, the interlayer must cover the surface uniformly with a high packing density. To address these issues, a multifunctional interlayer with broad compatibility that can reduce the energy offset of the perovskite/C_{60} interface, while being largely insensitive to the preparation condition (e.g., solution concentration) is needed.

In this work, we introduce 1,6-bis(acryloyloxy)-2,2,3,3,4,4,5,5-octafluorohexane (BA-8FH in short) as a multifunction interlayer at the perovskite/C_{60} interface, which enables a large deposition window from 1 mg/mL to 200 mg/mL with high reproducibility. BA-8FH features a low boiling point (~90 °C), lower than the annealing temperature of perovskite (100 °C). Thus, most deposited material will evaporate during the annealing process, leaving an approximate monolayer whose functional groups (F and acryloyloxy) have strong interactions with perovskite. Therefore, the molecule remains strongly bound to the perovskite surface despite its volatility. Ultraviolet photoelectron spectroscopy (UPS) reveals that BA-8FH improves the energy band alignment at the perovskite/C_{60} interface, resulting in substantially reduced nonradiative recombination with a longer carrier lifetime. Moreover, p-i-n structured devices with 1.58 eV perovskite bandgap delivered a PCE of 24.7% with a V_{OC} of 1.21 V and a FF of 84%. Encapsulated devices under an ambient atmosphere exhibited a T90 lifetime of over 1200 h after continuous MPP tracking. As such, this work provides a new strategy to solve the long-standing challenge of recombination losses at the perovskite/C_{60} interface, paving the way to eliminate the critical recombination losses of state-of-art perovskites.

To assess the overall effect of BA-8FH on photovoltaic performance, we first fabricated devices using the following stack: Glass/ITO/MeO-2PACz/$Cs_{0.05}(MA_{0.05}FA_{0.95})_{0.95}Pb(I_{0.95}Br_{0.05})_3$ perovskite treated with BA-8FH/C_{60}/BCP/Cu (Figure 1a). Further details are provided in the Supplementary Methods section. The PCE results of devices treated with different concentrations of BA-8FH are presented in Figure 1b, while the other performance parameters are presented in

https://doi.org/10.1021/acsenergylett.5c00615
ACS Energy Lett. 2025, 10, 2942−2951

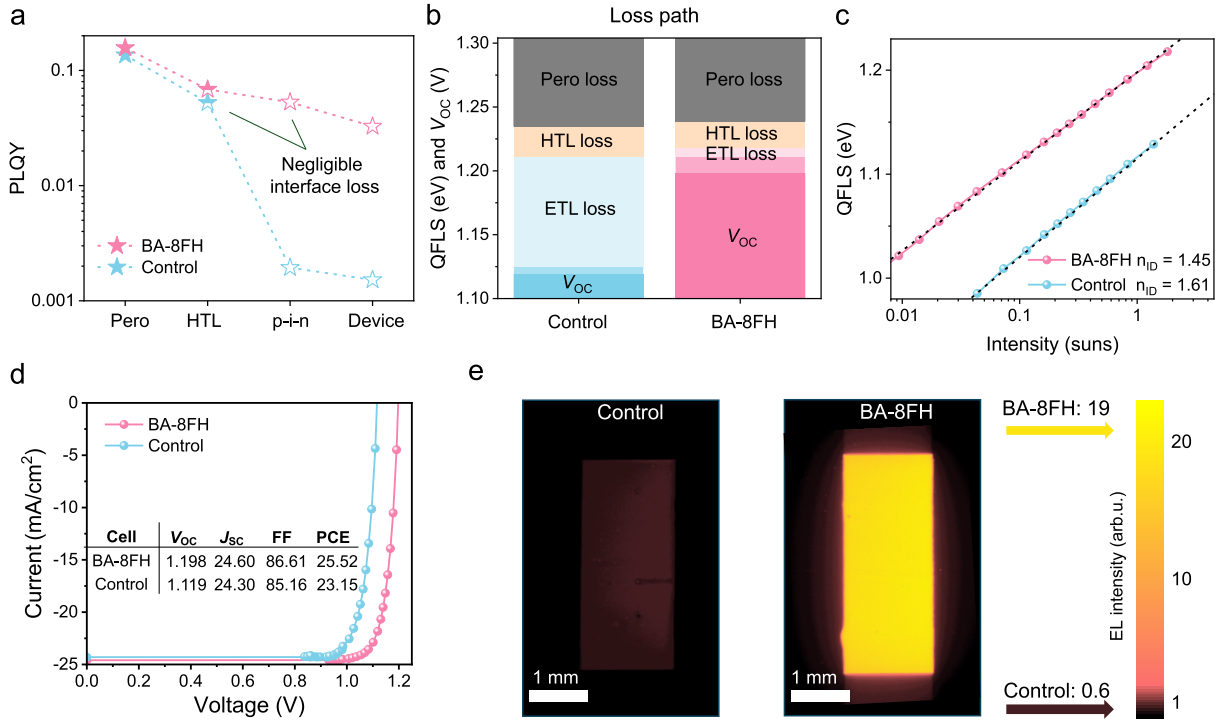

Figure 2. (a) PLQY results for quartz/perovskite, HTL/perovskite, HTL/perovskite/ETL films, and full devices with/without BA-8FH treatment, samples are labeled as Pero, HTL, p-i-n, and device, respectively. (b) Contributions to the overall voltage loss for control and BA-8FH treated samples. (c) Intensity-dependent quasi-Fermi level splitting (QFLS) measurements for control and BA-8FH devices, the ideality factors are listed. (d) Pseudo *J*–*V* curves from intensity-dependent QFLS measurements for control and BA-8FH treated devices with the parameters are listed as inset. (e) EL mapping for control and BA-8FH treated samples, the scale bar represents 1 mm. The average luminous intensity is calculated as a unitless value shown on the right.

Figure S1. Notably, the gradual improvement in PCE from 0 to ~30 mg/mL stems from a gradual improvement in V_{OC} and FF. Above this concentration, these parameters remain almost constant until 200 mg/mL. The short-circuit current density (J_{SC}) shows negligible fluctuations across various BA-8FH concentrations. This behavior is uncommon because, typically for solution-based coating processes, the solution concentration correlates positively with the resulting film thickness. For most passivation layers with poor conductivity, excessive thickness often leads to a significant increase in series resistance in solar cells, resulting in serious losses in FF and also V_{OC}, often accompanied by a QFLS-V_{OC} mismatch.[9,10,14−18] Hence, precise and narrow concentration windows are usually necessary to guarantee the effective operation of most passivation layers, balancing their intended effects with the introduction of series resistance. Notably, Figure 1a also shows that the cross-section of the BA-8FH layer processed from a 60 mg/mL solution is too thin (less than 5 nm) to be visible, while Figure S2 shows the comparison with the control sample. Considering BA-8FH's boiling point of only 90 °C, it is inferred that during spin-coating of BA-8FH layer and subsequent annealing, only the first BA-8FH monomolecular layer interacting directly with the perovskite surface remains stably adsorbed, while unadsorbed BA-8FH overlayers evaporate during annealing. Consequently, with the increase in BA-8FH concentration, an improvement in layer density is achieved while maintaining an ultrathin layer, thereby breaking the traditional dilemma of balancing density and keeping the passivation layer as thin as possible. We term this unique phenomenon, where the "passivation" effect of BA-8FH on device performance tends to saturate with increasing concentration, as depicted in Figure 1c, "saturated passivation". This saturation effect significantly widens the concentration window for the passivation layers, avoiding losses in fill factor or open-circuit voltage due to overly thick films. Moreover, this process, which involves the interaction of low-boiling-point substances with perovskites to adsorb monolayers of molecules, offers a new strategy to prepare ultrathin functional layers. We note that to achieve the best performance with minimum usage, the medium concentration (30 mg/mL) was selected for in-depth studies in the following and compared with a control sample.

To better understand the performance increase with increasing BA-8FH concentration, we performed photoluminescence quantum yield (PLQY) measurements and calculated the corresponding quasi-Fermi level splitting (QFLS) using

$$\mathrm{QFLS} = eV_{\mathrm{th}} \times \ln\left(\mathrm{PLQY} \times \frac{J_{\mathrm{G}}}{J_{0,\mathrm{rad}}}\right) \tag{2}$$

where e, J_{G} and $J_{0,\mathrm{rad}}$, are the elementary charge, the generated light and dark current, respectively (see Figure S3). To this end, we fabricated four configurations with either BA-8FH treatment or control: (1) perovskite films deposited on quartz glass, denoted as "pero"; (2) half stack samples with a configuration of glass/ITO/MeO-2PACz/perovskite, denoted as "HTL"; (3) C_{60} incorporated in "HTL" samples to form "p-i-n" samples (glass/ITO/MeO-2PACz/perovskite/C_{60}); and (4) full cells denoted as "device". As shown in Figure 2a and tabulated in Supplementary Table S1, "pero" samples exhibit similar PLQY values for control (13.6%) and BA-8FH (15.7%)

https://doi.org/10.1021/acsenergylett.5c00615
ACS Energy Lett. 2025, 10, 2942−2951

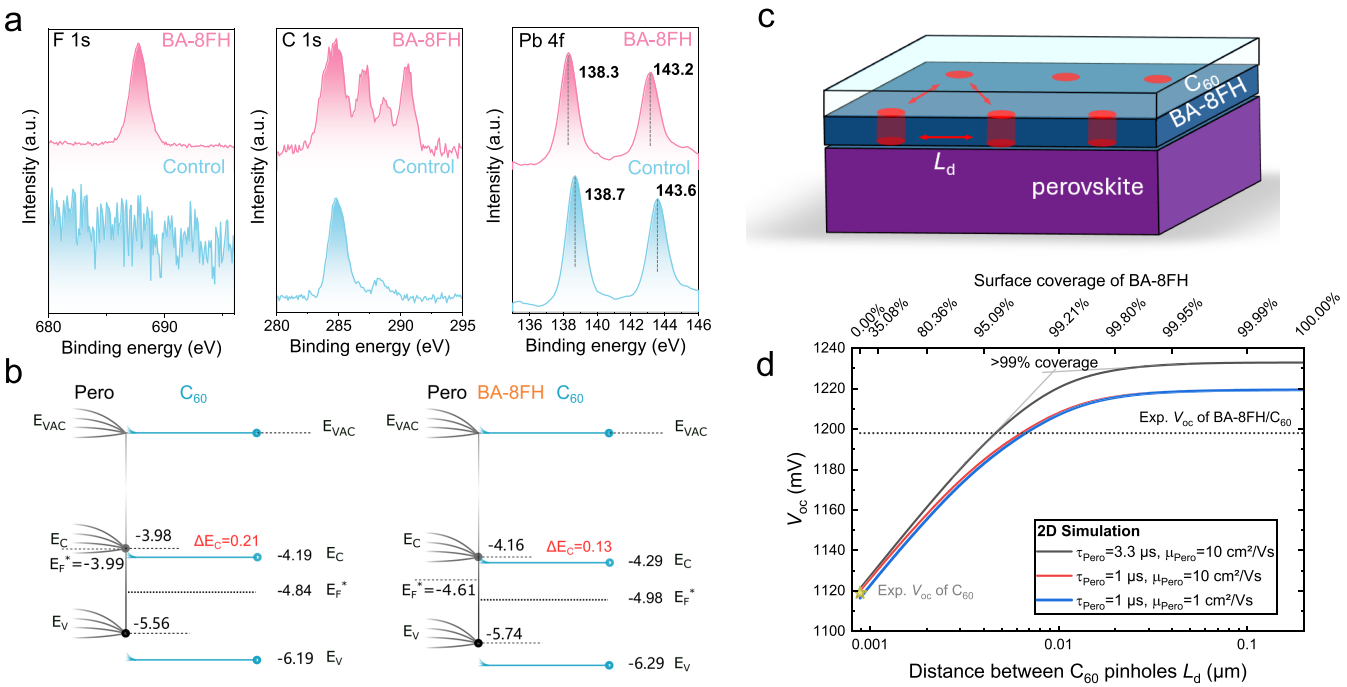

Figure 3. (a) High-resolution XPS spectra of F 1s, C 1s, and Pb 4f for control and BA-8FH-treated perovskite. (b) Energy level diagram at the perovskite/C_{60} interface for the control sample and BA-8FH treated sample upon aligning the vacuum level. (c) Schematic of 2D simulation. (d) Simulated V_{OC} as a function of distance (L_d) between areas without BA-8FH interlayer (pin-holes).

treated samples, with corresponding QFLS values of 1.235 and 1.239 eV, suggesting negligible surface passivation effects of BA-8FH on perovskite surface defects. PLQY and QFLS values of control (5.2%) and BA-8FH treated (6.9%) "HTL" samples closely follow the trend of those of "pero" samples, showing only a 7 meV difference for control and BA-8FH samples. In contrast, the PLQY and QFLS gap became significant after the incorporation of C_{60} in "p-i-n" samples and "devices" for the control samples. In particular, the PLQY of control "p-i-n" samples (0.19%) was reduced by approximately 27 times compared to its "HTL" counterpart, resulting in a QFLS loss of 86 mV, which indicates severe and predominant nonradiative recombination losses at the perovskite/C_{60} interface, consistent with previous observations and reports in the perovskite community.[9,10,14,19] However, for BA-8FH-treated "p-i-n" samples, the PLQY after C_{60} deposition (5.3%) is essentially unchanged compared to control "HTL" samples (5.2%), suggesting that the nonradiative recombination induced by C_{60} is eliminated. Plotting the QFLS of all tested samples, as depicted in Figure 2b further illustrates the contributions to the overall voltage loss in the devices. Finally, we note that compared with the widely used interlayers such as LiF or PEAI, the PLQY loss upon C_{60} deposition is substantially reduced for BA-8FH interlayer (Figure S4).

We also measured the QFLS for different light intensities from 0.001 suns to >1 suns. As shown in Figure 2c, the ideality factors of the control and BA-8FH-treated devices are 1.61 and 1.45, respectively. Furthermore, pseudo-*JV* curves of the devices were constructed to estimate the device performance potential under conditions neglecting transport losses. As depicted in Figure 2d, BA-8FH-treated devices exhibited a larger implied FF and V_{OC}, aligning with the FF improvement observed in the *JV* results. After eliminating transport losses, the efficiency potential of BA-8FH-treated devices reaches 25.52%. In order to gain a more intuitive and visual understanding of the suppressed nonradiative recombination processes at the perovskite/C_{60} interface, we performed electroluminescence (EL) mapping on a full device with/without BA-8FH. By injecting a current equivalent to the short-circuit current density, we recorded 2D luminescence images using a CCD camera. As shown in Figure 2e, after background subtraction, the average relative luminescence intensity of the control devices was 0.6 units per pixel, while that of the BA-8FH-treated devices was 19 units per pixel, which is almost 30 times higher than the control sample. This is consistent with the improved V_{OC} of the device (i.e., 80 mV, Figure 1a).

To understand the underlying reasons for the reduced recombination at the interface upon implementation of BA-8FH layer, we recorded SEM top-view images of perovskite films with and without BA-8FH treatment. As shown in Figure S5, similar grain size and morphologies between the two samples indicate that the BA-8FH layer was too thin to be visualized and had no apparent effect on the crystallization of perovskite films. To investigate the interaction between perovskite and BA-8FH, X-ray photoelectron spectroscopy (XPS) measurements were performed on control and BA-8FH-treated perovskite samples, as shown in the survey spectra (Figure S6a) and the detailed core level spectra (Figures 3a and Figure S6b). The prominent new peaks at 688.3 eV and emergent C signals at 287−292 eV in the BA-8FH sample, attributed to the F 1s, C═O, COOR, and F−C−F signals, respectively,[20] confirm the presence of BA-8FH on the perovskite surface. Considering the high vacuum conditions of XPS measurements, the detection of BA-8FH signals suggests it is stably adsorbed on the perovskite surface. Moreover, a significant 0.44 eV shift was observed for the Pb 4f core level and I 3d signals in the BA-8FH-treated sample compared to the control sample (Figure 3a and Figures S6), indicating a strong interaction between BA-8FH and the

https://doi.org/10.1021/acsenergylett.5c00615
ACS Energy Lett. 2025, 10, 2942−2951

perovskite. We note that clear perovskite signals are also detected in BA-8FH sample, which is consistent with a very thin layer of BA-8FH considering the very shallow information depth of XPS. By analyzing the intensity changes of the XPS signals using the methodology in refs.,[21] the thickness of BA-8FH (30 mg/mL) was estimated to be 8 Å, almost approaching a monolayer, which is consistent with our expectations.

We then performed He-1 Ultraviolet photoelectron spectroscopy (UPS) to investigate the band alignment at the perovskite/C_{60} interface with BA-8FH. The obtained spectra, including the fits, are shown in Figures S7 and S8. As observed for the core levels (Pb and I), we observe a 0.44 eV shift of the valence band maximum with respect to the substrate Fermi level. However, the work function shifts by 0.62 eV upon the introduction of BA-8FH. We interpret the core and energy level shift to an apparent reduced n-doping effect and the remaining 0.18 eV to a positive surface dipole (with the positive end next to the perovskite). The latter contributes to the overall shift of the work function and changes the energy alignment between the perovskite and C_{60} energy levels. To highlight the effect of the dipole on the energy level alignment, we align the vacuum levels and deduce the band diagram shown in Figure 3b. For the control sample, we observe that the conduction band edge of the perovskite is 210 meV higher than the LUMO level of C_{60}, consistent with previous studies. However, with the introduction of the BA-8FH layer, this mismatch decreases to 130 meV. Therefore, BA-8FH reduces the energy level difference at the perovskite/C_{60} interface by approximately 80 meV. We note this value is somewhat less than the interface dipole (180 meV) because we observed a small change in the C_{60} ionization potential (100 meV). Overall, this result is consistent with recent work on high-performance Si/perovskite tandem solar cells, where it was found that the molecular interlayer piperazinium iodide (PI) introduces a positive surface dipole of 350 meV, which compensates the energy offset between the perovskite and C_{60} of −310 meV for a 1.68 eV triple cation perovskite.[10] We note that although the energetic realignment appears to be small, it correlates quantitatively with the observed enhancements in V_{OC} and QFLS (~80 mV/meV). Moreover, this is consistent with device simulations, which were based on our previous model of high-performance p-i-n-type cells (Figure S9), leading us to believe that the reduction of the energy level difference by BA-8FH is the primary reason for the improved open-circuit voltage. Notably, our simulations also show that the FF improves with better energy alignment due to the reduced interfacial recombination shown in Figure S9. We note the latter is explained by the reduced minority carrier density at the interface with better energy alignment as discussed in ref 8. Nevertheless, the simulated FF improvement energy level alignment is rather small (~1%) compared to the FF improvement observed in the experiment (~5%), which indicates that the molecule also suppresses interfacial recombination. The latter is consistent with TRPL as noted below.

Therefore, we attribute a key effect of BA-8FH to a surface dipole, which reduces the perovskite/C_{60} energy level mismatch. Furthermore, we speculate that BA-8FH forms a very dense layer with increasing concentration (up to 30 mg/mL). To illustrate this point and to investigate the energy losses in the case of insufficient molecular coverage, we performed 2D point contact simulations using Sentaurus TCAD following Campa et al.[22] Specifically, we consider the voltage losses when small pinholes with a diameter of 1 nm exist with a variable pinhole distance (L_d), as illustrated in Figure 3c. The simulation parameters can be found in Table S2. These hypothetical pin-holes are areas where the perovskite is exposed to the energetically mismatched C_{60} layer with an energy level offset of 200 meV, i.e., not covered by the molecule. Figure 3d and Figure S10 show the calculated V_{OC} and FF as a function of L_d between areas without BA-8FH interlayer (pin-holes), for a high perovskite SRH lifetime of 1.1 μs (measured value, see below). The recombination properties at the Perovskite/C_{60} interface in the simulation were chosen to roughly match the V_{OC} with C_{60} fully exposed (1.1 V). Upon reducing the pinhole density, the V_{OC} reaches the experimental value of the BA-8FH treated device (1.2 V). Overall, the simulations show that the V_{OC} is not compromised for a pinhole spacing of 20 nm (regardless of the perovskite mobility being 1 $cm^2/(V\ s)$ or 10 $cm^2/(V\ s)$). We note that the 2D simulations include mobile ions; moreover, they highlight that negative ions accumulate below the B8-FH covered area, Figure S11. While this simulation is a simplification, it highlights 2 important points: (1) the energy levels must be well aligned and (2) the surface must be very well covered, which is likely achieved by the volatile nature of the molecule, which allows for using a high solvent concentration without increasing the thickness.

To gain deeper insight into the carrier dynamics across the perovskite/C_{60} interface, we conducted complementary transient surface photovoltage (tr-SPV) and transient photoluminescence (tr-PL), which allowed us to investigate the charge transfer kinetics. Tr-SPV measurements track the variation of the surface potential over a wide time domain, while tr-PL visualizes the charge carrier recombination kinetics. Therefore, they give complementary information on charge transfer, trapping, and recombination processes. The fast initial rise of the SPV signal usually yields information on the charge extraction processes, and the following decay of the signal is attributed to recombination processes. Moreover, insufficient charge extraction from the perovskite, poor selectivity, or recombination would slow down the rise time.[23]

Figure 4a shows the tr-SPV result for all samples with a repetition rate of excitation laser pulses of 125 kHz (which is the same rate as for TRPL measurements) and 1 kHz, which can avoid the reinjection of carriers from the transport layers to the perovskite during the pulse duration, and hence better assess extraction only (rise of negative signal). The result was further normalized to enable a visual comparison, as shown in Figure 4b. For the glass/pero sample, no significant tr-SPV signal was detected without any contact, which is expected as there is no carrier extraction. For the HTL/Pero sample control sample, the initial positive SPV signal at an early time scale of 1×10^{-7} s (shown in Figure S12 in more detail) indicates hole accumulation or trapping near the surface. In addition, the HTL/Pero sample shows a typical slow signal build-up, indicating typical slow hole extraction as reported in previous work. In contrast, the faster rise of the negative signal for the BA-8FH treated HTL/Pero sample likely corresponds to the faster flow of electrons to the perovskite surface (i.e., in the direction of the photocurrent), indicating electron extraction into the BA-8FH.[10,23] Moreover, the larger SPV amplitude for the BA-8FH treated sample indicates that fewer charge carriers are lost in the sample due to nonradiative recombination (Figure S12). After coating with C_{60}, the HTL/

https://doi.org/10.1021/acsenergylett.5c00615
ACS Energy Lett. 2025, 10, 2942−2951

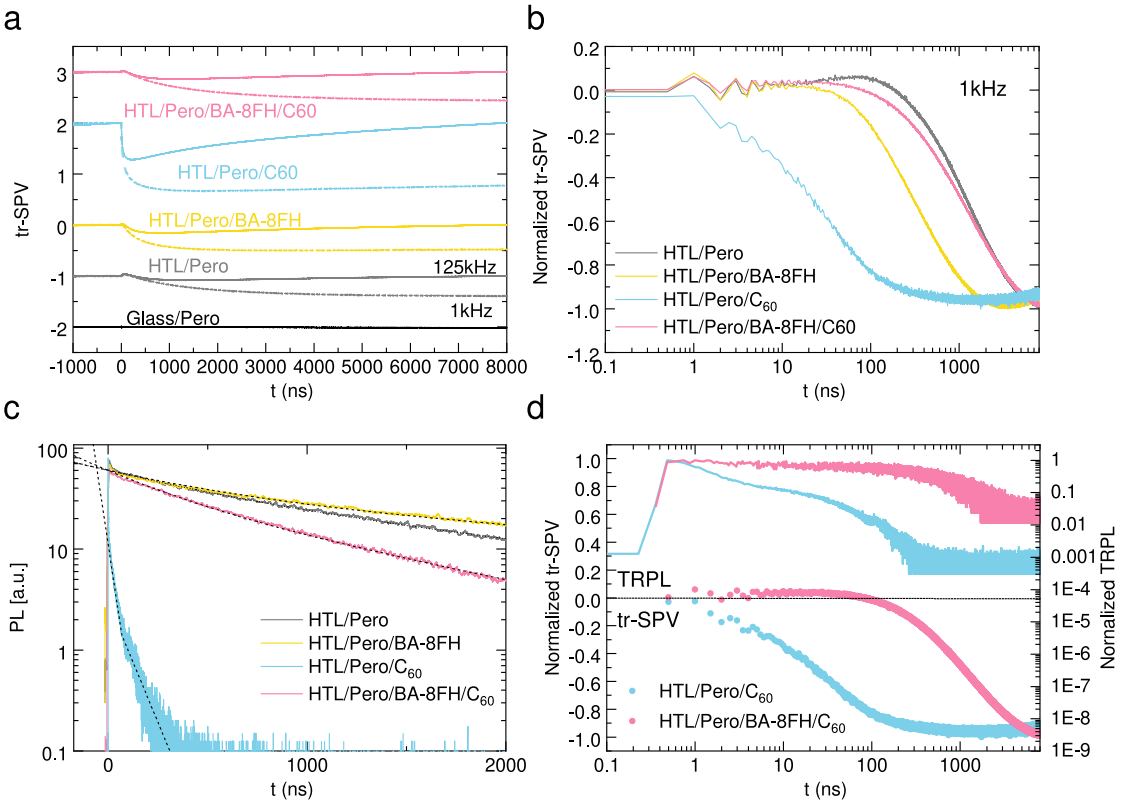

Figure 4. tr-SPV and TRPL results. (a) tr-SPV result for glass/pero, HTL/pero, HTL/pero/BA-8FH, HTL/pero/C_{60}, HTL/pero/BA-8FH/C_{60} samples, using a 515 nm laser at a frequency of 125 kHz (solid) and 1 kHz (dashed), respectively. The different traces were shifted vertically for better visibility (b) Normalized SPV for HTL/pero, HTL/pero/BA-8FH, HTL/pero/C_{60}, HTL/pero/BA-8FH/C_{60} samples at an excitation frequency of 1 kHz. (c) TRPL for HTL/pero, HTL/pero/BA-8FH, HTL/pero/C_{60}, HTL/pero/BA-8FH/C_{60} samples using a 515 nm laser at a frequency of 125 kHz. (d) Comparison of TRPL and tr-SPV for HTL/pero/C_{60} and HTL/pero/BA-8FH/C_{60} on the same time scale at an excitation frequency of 125 kHz and 1 kHz for TRPL and tr-SPV, respectively. Note all samples are on ITO/MeO-2PACz unless otherwise stated.

Pero/C_{60} sample leads to a fast electron extraction from the perovskite to the C_{60}. Surprisingly, the HTL/Pero/BA-8FH/C_{60} sample shows a much slower carrier extraction as compared with the direct C_{60} contact, even though C_{60}-only substantially increases the photocurrent extraction without BA-8FH. Therefore, with BA-8FH, the kinetic behavior of the electron extraction is very similar to the dynamics shown in the HTL/Pero sample, indicating balanced hole and electron transfer rates with BA-8FH treatment. Furthermore, we conduct resistance-dependent photovoltage (RPV) measurements on devices, which reveal the arrival time of both carriers at the device electrodes. As shown in Figure S13, BA-8FH samples demonstrate again a slower carrier extraction (transit) time at different pulse intensities, which is consistent with the tr-SPV result. Therefore, to our surprise, the introduction of BA-8FH slows the electron transfer rate. This result is unexpected considering that a faster electron transfer rate is generally beneficial, as there is less chance for recombination.

To better understand this, we turn our attention to the tr-PL analysis. As can be seen in Figure 4c, the neat perovskite on the HTL shows a long SRH decay time of 2100 ns (which is likely limited by the HTL layer, considering the PLQY results). We note that the decay time is half of the total carrier lifetime in case of high injection conditions, i.e., $\tau_{decay} = (\tau_n + \tau_p)/2$, and thus τ_{decay} can be seen as the average carrier lifetime.[13] After it is coated with C_{60}, significant nonradiative recombination leads to a 22× lower SRH lifetime of 95 ns. Consistently, with the above results, the C_{60} sample with BA-8FH shows a much smaller decrease of the SRH lifetime to 1100 ns, further confirming that a large reduction of nonradiative recombination is achieved. By merging the TRPL and tr-SPV data together in Figure 4d, we draw the conclusion that although the electron extraction into the C_{60} is slowed in the presence of BA-8FH, the extraction time is much longer than the average lifetime in the case of C_{60} but roughly similar in the case of BA-8FH/C_{60}. The slower electron transfer speed with BA-8FH treatment is likely associated with the isolating property of the BA-8FH layer, thus, a tunneling barrier may have formed. Overall, we conclude that suppressing interfacial recombination, thus realizing a longer carrier lifetime, plays a more crucial role than accelerating the electron transfer speed as long as it is not the limiting factor. In other words, the slower electron transit time will not impact the FF as long as it is still faster than the charge carrier lifetime, as well as the hole extraction time. Lastly, we note that we also performed a transient absorption spectrum (TAS) (2 uJ/cm^2) in a very narrow time domain of 0.1 to 7000 ps. Within this time window, we observe a more rapid decay in the perovskite/C60 sample compared to perovskite/BA-8FH/C60 and the HTL samples, which we attribute to faster interfacial recombination in the presence of C60, also considering that the transient SPV shows a slightly slower transfer of electrons to C_{60}. Detailed TAS results and kinetics and a comparison to TRPL are shown in Figures S14–S16 and Supplementary Note S1.

https://doi.org/10.1021/acsenergylett.5c00615
ACS Energy Lett. 2025, 10, 2942−2951

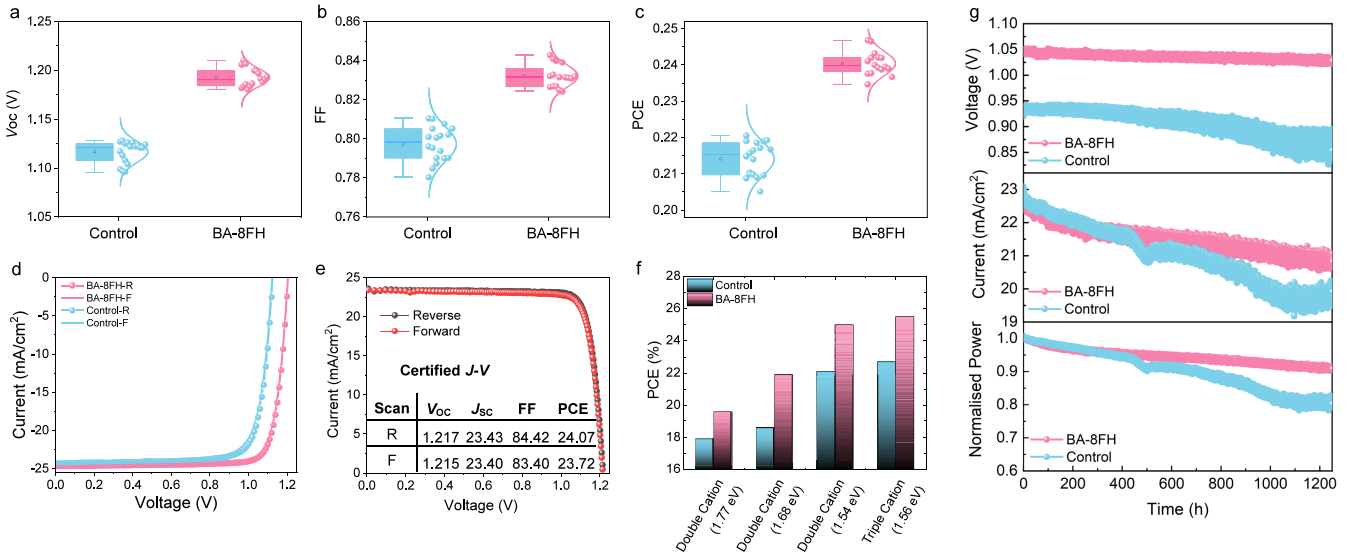

Figure 5. Parameters distribution of (a) V_{OC}, (b) FF, and (c) PCE for control and BA-8FH-treated cells under optimized perovskite. (d) $J-V$ curves of the champion cells under reverse and forward scan for control and BA-8FH treated samples. (e) Certified $J-V$ curves for BA-8FH treated device. (f) PCE enhancement with BA-8FH for different perovskite systems. (g) MPP tracking under a 1-sun equivalent intensity for control and BA-8FH treated devices, the V_{mmp} and J_{mpp} data are also listed for reference. The initial PCEs of the cells are 21.17% and 23.57% for control and BA-8FH-treated cells, respectively.

We then focus on the optimization of the devices based on the 30 mg/mL BA-8FH treatment using the following configuration: ITO/MeO-2PACz/perovskite/BA-8FH/C_{60}/BCP/Cu. Shown in Figure 5a–c and Figure S17 are the V_{OC}, J_{SC}, FF, and PCE distribution of control and BA-8FH treated solar cells. The surface treatment with BA-8FH improved V_{OC} (~80 mV) and FF (~3.5%), thus enhancing the PCE as compared with control cells by approximately 3.5%. The JV curves in reverse and forward scans obtained from the champion solar cells under standard AM 1.5G illumination (100 mW/cm^2) at a scan speed of 20 mV/s are shown in Figure 5d, and the corresponding photovoltaic parameters are summarized in Table 1. The device with BA-8FH treatment showed negligible hysteresis and reached a PCE of 24.7% in the reverse scan direction (mask area of 0.09 cm^2), with a V_{OC} of 1.21 V, J_{SC} of 24.7 mA/cm^2, FF of 83.1%. In comparison, the control device reached a PCE of 22.0% in reverse scan direction, with V_{OC} = 1.126 V, J_{SC} = 24.6 mA/cm^2, and FF = 80.1%. The best-performing BA-8FH-based cell also delivered a certified PCE of 24.1%, with a V_{OC} of 1.22 V, J_{SC} of 23.4 mA/cm^2, FF of 84.4% (Figure 5e and Figure S18). We note that these performances are somewhat below state-of-the-art values, with 27% reported recently in the NREL chart (unpublished). This high V_{OC} value enables us to reach a low nonradiative voltage loss of 87 mV for a 1.58 eV bandgap perovskite absorber, representing ~ 94% of the thermodynamic limit (1.304 V). Moreover, the integrated current density of the BA-8FH treated and control cells from the incident photon-to-current (IPCE) is 23.7 and 23.5 mAcm^{-2}, respectively, which matches the JV curves within a 5% error (Figure S19). We also measured the stabilized PCE at the maximum power point (MPP) over 600 s. As shown in Figure S20, the BA-8FH treated and control devices delivered stabilized PCE of 24.4% and 21.7%, respectively. The current drop in the initial 10s leads to a PCE drop for both devices, which can be associated with the ion movement in the perovskite layer.[24−26] To evaluate the impact of ionic loss of control and BA-8FH treated samples, scan-rate-dependent JV measurements were performed. This measurement allows us to estimate the efficiency loss due to the redistribution of mobile ions. At a very fast scan speed, the ion movement is essentially frozen, therefore, the ion-freeze PCE is obtained. As shown in Figure S21, a larger mismatch of PCE in high frequency indicates more ionic loss in control samples. This result can be attributed to the better interface quality in the BA-8FH sample which alleviates the ionic losses.[27]

Table 1. JV Parameters of the Champion Control and BA-8FH-Treated Samples under Reverse and Forward Scan

	scan	V_{OC} (V)	J_{SC} (mA/cm^2)	FF (%)	PCE (%)
control	reverse	1.126	24.36	80.05	21.96
	forward	1.121	24.38	78.03	21.33
BA-8FH	reverse	1.206	24.69	83.14	24.68
	forward	1.203	24.69	82.12	24.40

Moreover, to demonstrate the broad applicability of BA-8FH, we have studied additional perovskite systems with low- and wide-bandgaps for the potential implementation in tandem cells. For all perovskite systems, we observed similar trends of boosting V_{OC} and FF in device performance with BA-8FH treatment. For $FA_{0.95}Cs_{0.05}PbI_3$ (Figure S22, 1.54 eV), the PCE increases from 22.1% to 25.0%, for $Cs_{0.05}FA_{0.80}MA_{0.15}Pb(I_{0.75}Br_{0.25})_3$ (Figure S23, 1.68 eV), the PCE increases from 18.6% to 21.9%, for $FA_{0.8}Cs_{0.2}Pb(I_{0.6}Br_{0.4})_3$ (Figure S24, 1.77 eV), the PCE increases from 17.9% to 19.6%. We also repeated the measurements on a $Cs_{0.05}(MA_{0.05}FA_{0.95})_{0.95}Pb(I_{0.95}Br_{0.05})_3$ triple cation perovskite with a lower MACl and PbX_2 content, resulting in a slightly smaller bandgap (Figure S25, 1.56 eV) compared to the composition in the main text. Again, the PCE increases from 22.7% to 25.5%. All values are given in reverse scan direction and shown in Figure 5f.

Finally, we evaluated the operational stability of the encapsulated devices under continuous AM 1.5 illumination in an ambient atmosphere with ~ 40% relative humidity at ~40 °C (Figure 5g). The BA-8FH-treated cells retain ~90% of

https://doi.org/10.1021/acsenergylett.5c00615
ACS Energy Lett. 2025, 10, 2942−2951

their initial performance after 1200 h while the control cells retain ∼80% after the same time, consistent with the overall trend that reduced nonradiative correlates with better operational stability in perovskite cells.[28] Moreover, to investigate the device stability under high BA-8FH concentrations, we tracked the maximum power point of 3 different BA-8FH concentrations, 100, 60, and 30 mg/mL. We note, the result suggests no significant stability differences between the different BA-8FH concentrations (Figure S26). This is consistent with our above analysis, that the volatile nature of BA-FH leads to nonsignificant morphological differentiation across high-concentration regimes (60−100 mg/mL).

By introducing the volatile interlayer BA-8FH, we developed an effective "saturated passivation" method to reduce the nonradiative recombination at the perovskite/C_{60} interface, which is a long-standing challenge for inverted PSCs. When employed as an interfacial layer, it forms a functional monolayer, thus enabling a wide deposition window with regard to the solution concentration. We attribute the working mechanism of the BA-8FH layer to 2 main effects, 1) it decreases the energy misalignment between the perovskite and C_{60} layer without passivating the surface of perovskite, 2) it forms a dense interlayer that likely covers the perovskite surfaces very well (>99%), thereby preventing charge carrier funneling into the C_{60} with a lower energy level and associated interfacial losses. This allowed maintaining the high PLQY of the HTL/perovskite >5% upon the addition of the ETL. UPS and XPS measurements revealed that the reason for the improved energy alignment is a molecular dipole layer consistent with recent successful interlayers. Moreover, by performing tr-SPV, TRPL, as well as TAS measurements, we found that the electron extraction time is not limiting the performance as long as it is not shorter than the charge carrier lifetime. Overall, BA-8FH improves the triple cation device performance from 21% to 24.7% (certified 24.0%) as well as the T_{90} operational stability from 500 to 1200 h. Furthermore, the molecule is applicable to various perovskite compositions and bandgaps. Our study provides guidance for eliminating the interface recombination loss and provides a deeper understanding of the carrier dynamics, contributing toward the commercialization of inverted PSCs.

■ ASSOCIATED CONTENT

Supporting Information

The Supporting Information is available free of charge at https://pubs.acs.org/doi/10.1021/acsenergylett.5c00615.

Supplementary methods; Performance characteristics; Cross-section SEM images; Calculation of $J_{0,rad}$; Comparison of layer-by-layer PLQY with literature; Top-view SEM images; XPS survey spectra; UPS spectra of neat and perovskite/C60 samples w/and wo/BA-8FH; Drift diffusion simulations; 2D simulations of FF; Simulated ion accumulation in cross section; SPV transients; RPV transients; TAS kinetics of different stack layers; TAS spectra; Zoomed-in TRPL decays; J_{SC} statistics; Performance certification report; EQE spectra; Stabilized power output; Fast-hysteresis measurements; Performance results of $FA_{0.95}Cs_{0.05}PbI_3$, $Cs_{0.05}FA_{0.80}MA_{0.15}Pb(I_{0.75}Br_{0.25})_3$, $FA_{0.8}Cs_{0.2}Pb(I_{0.6}Br_{0.4})_3$, and $Cs_{0.05}(MA_{0.05}FA_{0.95})_{0.95}Pb(I_{0.95}Br_{0.05})_3$ perovskites; MPP tracking; PLQY/QFLS table; Supplementary Note on TAS; 2D simulation parameters; References (PDF)

■ AUTHOR INFORMATION

Corresponding Authors

Shuo Zhang − *Key Laboratory for Advanced Materials and Joint International Research Laboratory of Precision Chemistry and Molecular Engineering, Shanghai Key Laboratory of Functional Materials Chemistry, Frontiers Science Center for Materiobiology and Dynamic Chemistry, Institute of Fine Chemicals, School of Chemistry and Molecular Engineering, East China University of Science & Technology, 200237 Shanghai, China*; Email: shuozhang_ecust@163.com

Yongzhen Wu − *Key Laboratory for Advanced Materials and Joint International Research Laboratory of Precision Chemistry and Molecular Engineering, Shanghai Key Laboratory of Functional Materials Chemistry, Frontiers Science Center for Materiobiology and Dynamic Chemistry, Institute of Fine Chemicals, School of Chemistry and Molecular Engineering, East China University of Science & Technology, 200237 Shanghai, China*; orcid.org/0000-0003-3000-403X; Email: wu.yongzhen@ecust.edu.cn

Martin Stolterfoht − *Electronic Engineering Department, Chinese University of Hong Kong, Hong Kong, China*; orcid.org/0000-0002-4023-2178; Email: mstolterfoht@ee.cuhk.edu.hk

Authors

Fangyuan Ye − *Electronic Engineering Department, Chinese University of Hong Kong, Hong Kong, China; Key Laboratory for Advanced Materials and Joint International Research Laboratory of Precision Chemistry and Molecular Engineering, Shanghai Key Laboratory of Functional Materials Chemistry, Frontiers Science Center for Materiobiology and Dynamic Chemistry, Institute of Fine Chemicals, School of Chemistry and Molecular Engineering, East China University of Science & Technology, 200237 Shanghai, China; Shanghai Electric Hency Solar Technology Co., Ltd., Shanghai Electric Group Co., Ltd., 201199 Shanghai, China*

Felix Lang − *Institute of Physics and Astronomy, University of Potsdam, D-14476 Potsdam-Golm, Germany*; orcid.org/0000-0001-9711-380X

Meysam Raoufi − *Institute of Physics and Astronomy, University of Potsdam, D-14476 Potsdam-Golm, Germany*

Jianjun Liang − *Shanghai Electric Hency Solar Technology Co., Ltd., Shanghai Electric Group Co., Ltd., 201199 Shanghai, China*

Igal Levine − *Hebrew University of Jerusalem, Chemistry, 919040 Jerusalem, Israel*; orcid.org/0000-0003-0406-2922

Hannes Hempel − *Solar Energy Division, Helmholtz-Zentrum Berlin für Materialien und Energie GmbH, 12489 Berlin, Germany*

Dorothee Menzel − *Solar Energy Division, Helmholtz-Zentrum Berlin für Materialien und Energie GmbH, 12489 Berlin, Germany*; orcid.org/0000-0002-6303-8909

Fengshuo Zu − *Solar Energy Division, Helmholtz-Zentrum Berlin für Materialien und Energie GmbH, 12489 Berlin, Germany; Humboldt-Universitat zu Berlin, Institut fur Physik and IRIS Adlershof, 12489 Berlin, Germany*; orcid.org/0000-0002-5861-4887

https://doi.org/10.1021/acsenergylett.5c00615
ACS Energy Lett. 2025, 10, 2942−2951

Steve Albrecht − *Solar Energy Division, Helmholtz-Zentrum Berlin für Materialien und Energie GmbH, 12489 Berlin, Germany;* orcid.org/0000-0001-9962-9535
Lars Korte − *Solar Energy Division, Helmholtz-Zentrum Berlin für Materialien und Energie GmbH, 12489 Berlin, Germany;* orcid.org/0000-0002-9207-9048
Christoph Messmer − *Fraunhofer Institute for Solar Energy Systems and INATECH, Chair for Photovoltaic Energy Conversion, University of Freiburg, 79110 Freiburg, Germany*
Jonas Schön − *Fraunhofer Institute for Solar Energy Systems and INATECH, Chair for Photovoltaic Energy Conversion, University of Freiburg, 79110 Freiburg, Germany*
Stefan W. Glunz − *Fraunhofer Institute for Solar Energy Systems and INATECH, Chair for Photovoltaic Energy Conversion, University of Freiburg, 79110 Freiburg, Germany*
Thomas Unold − *Solar Energy Division, Helmholtz-Zentrum Berlin für Materialien und Energie GmbH, 12489 Berlin, Germany;* orcid.org/0000-0002-5750-0693
Norbert Koch − *Humboldt-Universitat zu Berlin, Institut fur Physik and IRIS Adlershof, 12489 Berlin, Germany;* orcid.org/0000-0002-6042-6447
Dieter Neher − *Institute of Physics and Astronomy, University of Potsdam, D-14476 Potsdam-Golm, Germany;* orcid.org/0000-0001-6618-8403
Dongting Ye − *Shanghai Electric Hency Solar Technology Co., Ltd., Shanghai Electric Group Co., Ltd., 201199 Shanghai, China*

Complete contact information is available at: https://pubs.acs.org/10.1021/acsenergylett.5c00615

Author Contributions

△F.Y. and S.Z. contributed equally to this paper.

Notes

The authors declare no competing financial interest.

■ ACKNOWLEDGMENTS

M.S. acknowledges the Vice-Chancellor Early Career Professorship Scheme from CUHK for funding. F.L. acknowledges funding from the Volkswagen Foundation via the Freigeist Program. The work from University of Freiburg was funded by the Deutsche Forschungsgemeinschaft (DFG, German Research Foundation) under SPP 2196: Perovskite Semiconductors: From Fundamental Properties to Devices, Project Number 402726906. Y.W. acknowledges funding support from the National Natural Science Foundation of China (22425502, 22179037, T2488302), Science and Technology Commission of Shanghai Municipality (24DX1400200), and Program of Introducing Talents of Discipline to Universities (B16017). S.Z. is thankful for the support from the Shanghai Sailing Program (24YF2708200) and the China Postdoctoral Science Foundation under Grant No. BX20240117.

■ REFERENCES

(1) Zai, H.; Yang, P.; Su, J.; Yin, R.; Fan, R.; Wu, Y.; Zhu, X.; Ma, Y.; Zhou, T.; Zhou, W.; Zhang, Y.; Huang, Z.; Jiang, Y.; Li, N.; Bai, Y.; Zhu, C.; Huang, Z.; Chang, J.; Chen, Q.; Zhang, Y.; Zhou, H. Wafer-Scale Monolayer MoS2 Film Integration for Stable, Efficient Perovskite Solar Cells. *Science* **2025**, *387* (6730), 186−192.
(2) Liu, S.; Li, J.; Xiao, W.; Chen, R.; Sun, Z.; Zhang, Y.; Lei, X.; Hu, S.; Kober-Czerny, M.; Wang, J.; Ren, F.; Zhou, Q.; Raza, H.; Gao, Y.; Ji, Y.; Li, S.; Li, H.; Qiu, L.; Huang, W.; Zhao, Y.; Xu, B.; Liu, Z.; Snaith, H. J.; Park, N.-G.; Chen, W. Buried Interface Molecular Hybrid for Inverted Perovskite Solar Cells. *Nature* **2024**, *632* (8025), 536−542.
(3) Ge, Y.; Zheng, L.; Wang, H.; Gao, J.; Yao, F.; Wang, C.; Li, G.; Guan, H.; Wang, S.; Cui, H.; Ye, F.; Shao, W.; Zheng, Z.; Yu, Z.; Wang, J.; Xu, Z.; Dai, C.; Ma, Y.; Yang, Y.; Guan, Z.; Liu, Y.; Wang, J.; Lin, Q.; Li, Z.; Li, X.; Ke, W.; Grätzel, M.; Fang, G. Suppressing Wide-Angle Light Loss and Non-Radiative Recombination for Efficient Perovskite Solar Cells. *Nat. Photonics* **2025**, *19*, 170−177.
(4) Yang, Y.; Chen, H.; Liu, C.; Xu, J.; Huang, C.; Malliakas, C. D.; Wan, H.; Bati, A. S. R.; Wang, Z.; Reynolds, R. P.; Gilley, I. W.; Kitade, S.; Wiggins, T. E.; Zeiske, S.; Suragtkhuu, S.; Batmunkh, M.; Chen, L. X.; Chen, B.; Kanatzidis, M. G.; Sargent, E. H. Amidination of Ligands for Chemical and Field-Effect Passivation Stabilizes Perovskite Solar Cells. *Science* **2024**, *386* (6724), 898−902.
(5) Green, M. A.; Dunlop, E. D.; Yoshita, M.; Kopidakis, N.; Bothe, K.; Siefer, G.; Hao, X.; Jiang, J. Y. Solar Cell Efficiency Tables (Version 65). *Progress in Photovoltaics: Research and Applications* **2025**, *33* (1), 3−15.
(6) Ma, C.; Park, N.-G. A Realistic Methodology for 30% Efficient Perovskite Solar Cells. *Chem.* **2020**, *6* (6), 1254−1264.
(7) Suchan, K.; Jacobsson, T. J.; Rehermann, C.; Unger, E. L.; Kirchartz, T.; Wolff, C. M. Rationalizing Performance Losses of Wide Bandgap Perovskite Solar Cells Evident in Data from the Perovskite Database. *Adv. Energy Mater.* **2024**, *14* (5), No. 2303420.
(8) Warby, J.; Zu, F.; Zeiske, S.; Gutierrez-Partida, E.; Frohloff, L.; Kahmann, S.; Frohna, K.; Mosconi, E.; Radicchi, E.; Lang, F.; Shah, S.; Peña-Camargo, F.; Hempel, H.; Unold, T.; Koch, N.; Armin, A.; De Angelis, F.; Stranks, S. D.; Neher, D.; Stolterfoht, M. Understanding Performance Limiting Interfacial Recombination in Pin Perovskite Solar Cells. *Adv. Energy Mater.* **2022**, *12* (12), No. 2103567.
(9) Liu, J.; De Bastiani, M.; Aydin, E.; Harrison, G. T.; Gao, Y.; Pradhan, R. R.; Eswaran, M. K.; Mandal, M.; Yan, W.; Seitkhan, A.; Babics, M.; Subbiah, A. S.; Ugur, E.; Xu, F.; Xu, L.; Wang, M.; Rehman, A. ur; Razzaq, A.; Kang, J.; Azmi, R.; Said, A. A.; Isikgor, F. H.; Allen, T. G.; Andrienko, D.; Schwingenschlögl, U.; Laquai, F.; De Wolf, S. Efficient and Stable Perovskite-Silicon Tandem Solar Cells through Contact Displacement by MgFx. *Science* **2022**, *377* (6603), 302−306.
(10) Mariotti, S.; Köhnen, E.; Scheler, F.; Sveinbjörnsson, K.; Zimmermann, L.; Piot, M.; Yang, F.; Li, B.; Warby, J.; Musiienko, A.; Menzel, D.; Lang, F.; Keßler, S.; Levine, I.; Mantione, D.; Al-Ashouri, A.; Härtel, M. S.; Xu, K.; Cruz, A.; Kurpiers, J.; Wagner, P.; Köbler, H.; Li, J.; Magomedov, A.; Mecerreyes, D.; Unger, E.; Abate, A.; Stolterfoht, M.; Stannowski, B.; Schlatmann, R.; Korte, L.; Albrecht, S. Interface Engineering for High-Performance, Triple-Halide Perovskite−Silicon Tandem Solar Cells. *Science* **2023**, *381* (6653), 63−69.
(11) Remmerswaal, W. H. M.; van Gorkom, B. T.; Zhang, D.; Wienk, M. M.; Janssen, R. A. J. Quantifying Non-Radiative Recombination in Passivated Wide-Bandgap Metal Halide Perovskites Using Absolute Photoluminescence Spectroscopy. *Adv. Energy Mater.* **2024**, *14* (12), No. 2303664.
(12) Menzel, D.; Al-Ashouri, A.; Tejada, A.; Levine, I.; Guerra, J. A.; Rech, B.; Albrecht, S.; Korte, L. Field Effect Passivation in Perovskite Solar Cells by a LiF Interlayer. *Adv. Energy Mater.* **2022**, *12* (30), No. 2201109.
(13) Kirchartz, T.; Márquez, J. A.; Stolterfoht, M.; Unold, T. Photoluminescence-Based Characterization of Halide Perovskites for Photovoltaics. *Adv. Energy Mater.* **2020**, *10* (26), No. 1904134.
(14) Ye, F.; Zhang, S.; Warby, J.; Wu, J.; Gutierrez-Partida, E.; Lang, F.; Shah, S.; Saglamkaya, E.; Sun, B.; Zu, F.; Shoaee, S.; Wang, H.; Stiller, B.; Neher, D.; Zhu, W.-H.; Stolterfoht, M.; Wu, Y. Overcoming C60-Induced Interfacial Recombination in Inverted Perovskite Solar Cells by Electron-Transporting Carborane. *Nat. Commun.* **2022**, *13* (1), 7454.
(15) Jiang, Q.; Zhao, Y.; Zhang, X.; Yang, X.; Chen, Y.; Chu, Z.; Ye, Q.; Li, X.; Yin, Z.; You, J. Surface Passivation of Perovskite Film for Efficient Solar Cells. *Nat. Photonics* **2019**, *13* (7), 460−466.

(16) Peng, J.; Khan, J. I.; Liu, W.; Ugur, E.; Duong, T.; Wu, Y.; Shen, H.; Wang, K.; Dang, H.; Aydin, E.; Yang, X.; Wan, Y.; Weber, K. J.; Catchpole, K. R.; Laquai, F.; De Wolf, S.; White, T. P. A Universal Double-Side Passivation for High Open-Circuit Voltage in Perovskite Solar Cells: Role of Carbonyl Groups in Poly(Methyl Methacrylate). *Adv. Energy Mater.* **2018**, *8* (30), No. 1801208.
(17) Wang, Q.; Dong, Q.; Li, T.; Gruverman, A.; Huang, J. Thin Insulating Tunneling Contacts for Efficient and Water-Resistant Perovskite Solar Cells. *Adv. Mater.* **2016**, *28* (31), 6734−6739.
(18) Chen, H.; Maxwell, A.; Li, C.; Teale, S.; Chen, B.; Zhu, T.; Ugur, E.; Harrison, G.; Grater, L.; Wang, J.; Wang, Z.; Zeng, L.; Park, S. M.; Chen, L.; Serles, P.; Awni, R. A.; Subedi, B.; Zheng, X.; Xiao, C.; Podraza, N. J.; Filleter, T.; Liu, C.; Yang, Y.; Luther, J. M.; De Wolf, S.; Kanatzidis, M. G.; Yan, Y.; Sargent, E. H. Regulating Surface Potential Maximizes Voltage in All-Perovskite Tandems. *Nature* **2023**, *613* (7945), 676−681.
(19) Stolterfoht, M.; Wolff, C. M.; Márquez, J. A.; Zhang, S.; Hages, C. J.; Rothhardt, D.; Albrecht, S.; Burn, P. L.; Meredith, P.; Unold, T.; Neher, D. Visualization and Suppression of Interfacial Recombination for High-Efficiency Large-Area Pin Perovskite Solar Cells. *Nat. Energy* **2018**, *3* (10), 847−854.
(20) Chen, X.; Wang, X.; Fang, D. A Review on C1s XPS-Spectra for Some Kinds of Carbon Materials. *Fullerenes, Nanotubes and Carbon Nanostructures* **2020**, *28* (12), 1048−1058.
(21) Ridzel, O. Yu.; Astašauskas, V.; Werner, W. S. M. Low Energy (1−100 eV) Electron Inelastic Mean Free Path (IMFP) Values Determined from Analysis of Secondary Electron Yields (SEY) in the Incident Energy Range of 0.1−10 keV. *J. Electron Spectrosc. Relat. Phenom.* **2020**, *241*, No. 146824.
(22) Čampa, A.; Smole, F.; Folchert, N.; Wietler, T.; Min, B.; Brendel, R.; Topič, M. Detailed Analysis and Understanding of the Transport Mechanism of Poly-Si-Based Carrier Selective Junctions. *IEEE Journal of Photovoltaics* **2019**, *9* (6), 1575−1582.
(23) Levine, I.; Al-Ashouri, A.; Musiienko, A.; Hempel, H.; Magomedov, A.; Drevilkauskaite, A.; Getautis, V.; Menzel, D.; Hinrichs, K.; Unold, T.; Albrecht, S.; Dittrich, T. Charge Transfer Rates and Electron Trapping at Buried Interfaces of Perovskite Solar Cells. *Joule* **2021**, *5* (11), 2915−2933.
(24) Tress, W.; Marinova, N.; Moehl, T.; Zakeeruddin, S. M.; Nazeeruddin, M. K.; Grätzel, M. Understanding the Rate-Dependent J−V Hysteresis, Slow Time Component, and Aging in CH3NH3PbI3 Perovskite Solar Cells: The Role of a Compensated Electric Field. *Energy Environ. Sci.* **2015**, *8* (3), 995−1004.
(25) Richardson, G.; O'Kane, S. E. J.; Niemann, R. G.; Peltola, T. A.; Foster, J. M.; Cameron, P. J.; Walker, A. B. Can Slow-Moving Ions Explain Hysteresis in the Current−Voltage Curves of Perovskite Solar Cells? *Energy Environ. Sci.* **2016**, *9* (4), 1476−1485.
(26) Domanski, K.; Roose, B.; Matsui, T.; Saliba, M.; Turren-Cruz, S.-H.; Correa-Baena, J.-P.; Carmona, C. R.; Richardson, G.; Foster, J. M.; De Angelis, F.; Ball, J. M.; Petrozza, A.; Mine, N.; Nazeeruddin, M. K.; Tress, W.; Gratzel, M.; Steiner, U.; Hagfeldt, A.; Abate, A. Migration of Cations Induces Reversible Performance Losses over Day/Night Cycling in Perovskite Solar Cells. *Energy Environ. Sci.* **2017**, *10* (2), 604−613.
(27) Thiesbrummel, J.; Shah, S.; Gutierrez-Partida, E.; Zu, F.; Peña-Camargo, F.; Zeiske, S.; Diekmann, J.; Ye, F.; Peters, K. P.; Brinkmann, K. O.; Caprioglio, P.; Dasgupta, A.; Seo, S.; Adeleye, F. A.; Warby, J.; Jeangros, Q.; Lang, F.; Zhang, S.; Albrecht, S.; Riedl, T.; Armin, A.; Neher, D.; Koch, N.; Wu, Y.; Le Corre, V. M.; Snaith, H.; Stolterfoht, M. Ion-Induced Field Screening as a Dominant Factor in Perovskite Solar Cell Operational Stability. *Nat. Energy* **2024**, *9* (6), 664−676.
(28) Hartono, N. T. P.; Köbler, H.; Graniero, P.; Khenkin, M.; Schlatmann, R.; Ulbrich, C.; Abate, A. Stability Follows Efficiency Based on the Analysis of a Large Perovskite Solar Cells Ageing Dataset. *Nat. Commun.* **2023**, *14* (1), 4869.

https://doi.org/10.1021/acsenergylett.5c00615
ACS Energy Lett. 2025, 10, 2942−2951